Pharmacophore

ISSN-2229-5402

Journal home page: http://www.pharmacophorejournal.com

IMPURITY D OF ANTICANCER DRUG FULVESTRANT AS A POTENTIAL MULTIFUNCTIONAL INHIBITOR FOR THE MARBURG VIRUS

Haoqi Wang[1], Nirmitee Mulgaonkar[1], Samavath Mallawarachchi[1], Sandun Fernando[1*]

1. Biological and Agricultural Engineering, Texas A&M University, College Station TX, USA.

ARTICLE INFO

Received:
21 Mar 2021
Received in revised form:
24 May 2021
Accepted:
27 May 2021
Available online:
28 Jun 2021

Keywords: Marburg virus, VP35, Fulvestrant impurity D, Anticancer drug

ABSTRACT

A commonality between viruses and cancer is their ability to seize cellular machinery to rapidly proliferate while suppressing the host's innate immune response. Using probe molecules, specific sites within the virion protein 35 (VP35) of the Marburg virus that have a high affinity to dsRNA (also known as the interferon inhibitory domain, IID), RNA-dependent RNA polymerase (RdRp), and nucleoside triphosphates (NTPs) were identified *in silico*. Using the dsRNA- binding site as the target, three potential drug molecules FID, CBSMA, and DOCHE were screened. We discovered that FID has a unique ability to simultaneously bind to all the three key binding domains with high affinity – a property that none of the other screened drug-like candidates possessed. The ability of FID to bind onto multiple domains of VP35 is significant since this provides the potential to thwart a viral infection from several fronts simultaneously using a single drug to combat rapidly mutating viruses.

To Cite This Article: Wang H, Mulgaonkar N, Mallawarachchi S, Fernando S. Impurity D of Anticancer Drug Fulvestrant as a Potential Multifunctional Inhibitor for the Marburg Virus. Pharmacophore. 2021;12(3):1-11. https://doi.org/10.51847/2hVQ1HunuP

Introduction

Marburg virus (MV), which causes Marburg virus disease (MVD), a form of viral hemorrhagic fever, is a Category-A bioagent [1, 2] that can cause unprecedented devastation. MVD was first discovered in 1967 when the importation of infected monkeys from Uganda caused epidemics in Germany and Yugoslavia [3]. Since then, several outbreaks of MVD have been reported, with the last outbreak occurring in 2017 in Kween district, Uganda [4-7]. MV is a filovirus - the same family that causes Ebola virus disease, and these viruses are among the most virulent human pathogens known; with the most recent outbreaks showing high pathogenicity and an extremely high human fatality rate between 23 to 90% [8, 9]. The main causes of fatality by MV include internal hemorrhage and organ failure [9-11]. Unfortunately, there are no licensed vaccines nor drugs available to treat an infection caused by the MV [12-14].

To confront MV, there are only a handful of proteins to target: NP (nucleoprotein), VP35 (polymerase cofactor), VP40 (matrix protein) [15], GP (glycoprotein), VP24 (minor matrix protein) [16], VP30 (transcription factor) [17], and L (RNA-dependent RNA polymerase [18], RdRp) and yet, no inhibitor has been uncovered that can effectively suppress viral replication. Moreover, in MV, VP35 and VP40 proteins show immunosuppressive properties [19-21], adding another layer of defense from being attacked by our immune system. The VP35 present in both Marburg and Ebola viruses is a multifunctional protein that acts as a polymerase cofactor and a viral protein chaperone [19, 22, 23]. In addition, it can also act as an antagonist to the natural immune responses, including interferon (IFN) production and protein kinase R activation [24]. Due to its multifunctionality, it is believed that obstructing the RNA-dependent polymerase cofactor VP35 could be one of the most viable and yet unexplored approaches to silencing filovirus replication.

VP35 contains a central oligomerization domain with a predicted coiled-coil motif (residues 70-120 on sequence UniProtKB - P35259 (VP35_MABVM)) essential for RNA polymerase function and homo-oligomerization of the protein, a chaperoning peptide at the N-terminal that acts as a chaperone for viral proteins and an interferon (IFN) inhibitory domain (IID) at the C-terminal end (residues 204-329) that binds dsRNA [19]. VP35-mediated IFN antagonism correlates with double-stranded RNA (dsRNA) binding activity. The binding of VP35 IID to dsRNA can block the detection of dsRNA by immune sensors such as RGI-I and MDA5, thus inhibiting interferon production [19, 25]. Contrary to the Ebola virus VP35 IID, which has a

Corresponding Author: Sandun Fernando; Biological and Agricultural Engineering, Texas A&M University, College Station TX. E-mail: sfernando@tamu.edu.

higher affinity towards the blunt ends of dsRNA, MV IID tends to coat the backbone of dsRNA [26]. It is also able to inhibit phosphorylation of interferon regulatory factor 3 (IRF3) [27]. Since all these domains are critical for viral proliferation and virulence, the antiviral activity against MV could be achieved by targeting either of the domains above.

Isolating the RdRp binding domain of VP35 helps to understand the protein functions. RdRp catalyzes the transcription, capping, and polyadenylation of viral mRNAs. Specifically, the polymerase catalyzes negative single-stranded viral RNA ((-)ssRNA) replication. The template consisted of the viral RNA tightly encapsulated by the nucleoprotein (NP). The viral RdRp binds the promoter region at the 3' terminus of genomic RNA and proceeds with the transcription of viral mRNA. The viral phosphoprotein acts as a processivity factor. Capping of mRNA is concomitant with the initiation of mRNA transcription, and is done by GDP polyribonucleotidyl transferase (PRNTase) enzyme once the nascent RNA chain reaches a length of a few nucleotides. Ribose 2'-O-methylation of viral mRNA cap precedes and facilitates subsequent guanine-N-7 methylation; the viral polymerase carries both activities. Polyadenylation of mRNAs occurs by a stuttering mechanism at a slippery stop site present at the end of viral genes. Once the mRNA transcription is finished, the polymerase is able to resume transcription of the downstream gene. The reactions involved, and thus could be disrupted, by RdRp suppression are as follows [28]:

- Nucleoside triphosphate + RNA(n) → diphosphate + RNA(n+1)
- S-adenosyl-L-methionine + G(5')pppR-RNA → S-adenosyl-L-homocysteine + m_7G(5')pppR-RNA
- 5'-triphospho-mRNA + GDP → diphosphate + guanosine 5'-triphospho-mRNA
- S-adenosyl-L-methionine + a 5'-(N(7)-methyl 5'-triphosphoguanosine)-(2'-O-methyl-purine-ribonucleotide)-(ribonucleotide)-[mRNA] → S-adenosyl-L-homocysteine + a 5'-(N(7)-methyl 5'-triphosphoguanosine)-(2'-O-methyl-purine-ribonucleotide)-(2'-O-methyl-ribonucleotide)-[mRNA]

There is only a limited amount of research done on the discovery of drugs targeting MV VP35 [22]. One study reports the use of synthetic antibody sFab H3 as a specific inhibitor of MV IID [29], and some studies were done using non-human primates present siRNA and PMOplus as potential filovirus VP35 inhibitors [30]. However, these studies are still at the preliminary stage.

This work aims to identify inhibitors that have a high potential to impede viral replication and immune suppression via VP35 silencing by analyzing interactions between impinging ligands and the dynamically changing receptor via molecular dynamics (MD) simulations.

Materials and Methods

Protein Sequence Analysis

The VP35 protein in MV comprises of a central oligomerization domain (residues 70-120 on sequence UniProtKB - P35259 (VP35_MABVM)) essential for RNA polymerase function [19] and an interferon (IFN) inhibitory domain (IID) at the C-terminal end (residues 204-329) that binds dsRNA. VP35-mediated IFN antagonism correlates with the binding activity of double-stranded RNA (dsRNA). The central oligomerization domain has a known RNA polymerase function which is called the RNA binding domain (RBD). Experiments have shown that VP35 binds to dsRNA to avoid detection by the immune system. The crystal structure of the coiled-coil region of VP35 (PDB: 5TOH) [19] and RBD in MV VP35 bound with dsRNA (PDB: 4GHA) [26] obtained by X-ray diffraction was available in the Protein Data Bank. Residues 261 to 329 from this structure were predicted to interact with the RBD. Computational predictions of the three-dimensional structure of proteins were constructed using comparative homology modeling techniques. Since the crystal structure of the Marburg virus L-protein has not yet been solved, a homology model was developed using the amino-acid sequence UniProtKB - P31352 (L_MABVM) [31] to ascertain the binding behavior of VP35 on RdRp protein. The antiviral activity could be achieved by targeting either of the domains above.

RNA-dependent RNA Polymerase (Rdrp Protein) Interactions with VP35

The modeled RdRp protein and VP35 binding phenomena were resolved using the ZDOCK [32] server using the IID containing subunit (4GHA-chain A) and coiled-coil region (5TOH) of VP35 as the receptor and RdRp as the ligand and vice versa. ZDOCK is an interactive server that performs a rigid-body search for predicting docked conformations of two interacting proteins.

Double and Single-Stranded RNA and NTP Interactions on VP35

RNA-interacting complexes were prepared by the default AutoDock Vina protocol, where RNA is considered as the ligand and VP35 as the receptor [33]. Two grid boxes were made based on the two known active sites of VP35, the IID, and RdRp binding pockets. Interaction diagrams and contacted amino acids were analyzed in MGLtools 4 [34].

The ligandability of NTP on VP35 was analyzed via AutoDock Vina [35]. The protocols were same as given above.

Druggability Assessment

Then, a druggability analysis [36] was done to ascertain the feasibility of using VP35 as a receptor that would respond to potential drugs by running 40 ns NAMD [37] simulations of the receptor in the presence of a solution containing small

organic probe molecules. The probes, which are the representatives of typical drug-like molecules consisted of isopropanol (70%), acetamide (10%), isobutene (10%), isopropylamine (5%), and acetate (5%). The druggability of MV VP35 was assessed to locate the presence of individual or clusters of hot spots indicative of a potential drug binding site. The equilibrated system consisted of 2800 water and 140 probe molecules (i.e., 98 isopropanol, 14 acetamide, 14 isobutene, 07 isopropylamines, and 07 acetates,). Chloride ions were added to make the system charge neutral.

Pharmacophore Identification

Enhanced Ligand Exploration and Interaction Recognition Algorithm (ELIXIR-A) [38-41] (ELIXIR-A) was used for isolating pharmacophore points based on the analyses of interactions between VP35 and probe molecules. ELIXIR-A is an in-house pharmacophore screening algorithm that recognizes pharmacophoric features, i.e., the ensemble of steric, electrostatic, and hydrophobic properties that are crucial for optimum supramolecular interactions with the target receptor to inhibit its biological activity. The probe molecules were converted to pharmacophores using the ELIXIR-A VMD plugin. These pharmacophores were used for further compound screening.

Compound Screening and Verification

With the pharmacophore information obtained from ELIXIR-A, potential compounds were screened using the ZINCPharmer software [42] from the ZINC15 database [43]. Structure-guided pharmacophore-based screening focuses on identifying ligand conformations with potential pharmacophore features based on the functional groups (side chains of amino acids) present at the binding site of the receptor. The binding of molecules having a minimum of three pharmacophore points was validated *in silico* via AutoDock Vina using a molecular docking protocol. Vina uses a scoring function to evaluate several docked orientations for each small molecule and reports only the nine most stable conformations with the most negative binding score (i.e., the highest binding affinity). The binding of the compound having the highest affinity amongst those screened was further evaluated via MD simulations.

Intermolecular Interaction Analysis from MD Simulations

The screened ligands were selected to study the possible mode of action (MOA) on the receptor after the docking simulation. The MD simulations were performed on the Schrödinger Desmond platform [44]. The system was solvated in an orthorhombic box using the Simple Point-Charge (SPC) solvent model with a buffer distance of 10 Å. The protein and ligand structures were optimized using Schrödinger's Protein Preparation Wizard [45]. The docked complexes were prepared by Glide [46]. The free N and C termini of the protein were capped for stabilizing the protein structure. All the missing hydrogens were added, and hydrogen bonds (H-bonds) were optimized. The strained minimization was performed with the OPLS3e force field [47]. Prior to simulation, each system was minimized using Schrödinger Desmond's default relaxation protocol. The simulations were performed under the OPLS3e force field. For equilibration, the system heavy atoms were first minimized with restrains under 10K, then increasing the temperature to 300K with restrains and the final relaxation step under 300K Normal Pressure and Temperature (NPT) ensemble. After relaxation, the simulations were carried out under the NPT ensemble at 300K and 1.01325 bar pressure for 20 ns. The recording interval was 20ps and 1000 frames were saved. Post simulation trajectory analyses were performed by Schrödinger Simulation Interactions Diagram (SID).

Results and Discussion

RNA-dependent RNA Polymerase (RdRp protein) Interactions with VP35

The interactions between RdRp and VP35 proteins were resolved using ZDOCK server **(Figure 1)**. For ease of interpretation, we have kept the VP35 projection coordinates constant to the extent possible throughout the document.

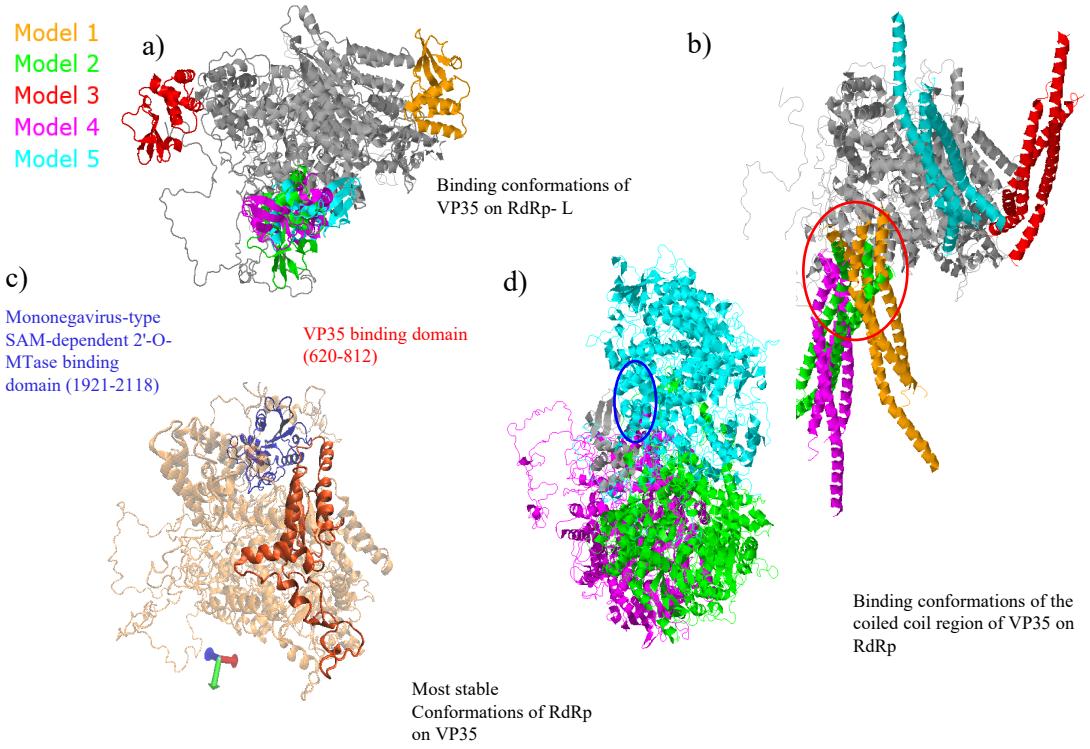

Figure 1. a) Binding conformations of VP35 on RNA-dependent RNA polymerase – L (RdRp protein); b) Multiple conformations of coiled coil region of VP35 on RdRp protein; c) Mononegavirus-type SAM-dependent 2'-O-MTase binding domain and VP35 domains on RdRp. Based on the analysis, the likely site of MV VP35 binding location on RdRp is demarcated with a red circle while the RdRp binding site on VP35 is demarcated with a blue circle.

The analysis generated several binding conformations of VP35 onto RdRp **(Figure 1a)**. A simulation coiled-coil region of VP35 further confirmed the VP35 binding site on RdRp as depicted in **Figure 1b** with multiple conformations binding at the vicinity of residues 620-812 of RdRp as reported previously **(Figure 1c)**. Simulations predicted two possible sites for RdRp binding on VP35 and based on further analysis the site demarcated in a blue circle spanning residues 210-299 was assigned as the RdRp binding domain on VP35 as depicted in **Figure 1d**.

Double and Single-Stranded RNA Interactions on VP35

To isolate RNA binding sites, a simulation of a double-stranded12-base-pair RNA (dsRNA) with RNA-dependent Polymerase MV VP35 protein (Lake Victoria strain Musoke 80; PDB: 4GHA) was performed. This initial simulation predicted two sites that have a high affinity to dsRNA on VP35, consistent with that resulted from RdRp and VP35 simulations. After comparing the simulation output with the actual crystal structure of dsRNA-interfaced Marburg VP35 (PDB: 4GHA), the RdRp binding site and dsRNA binding sites were confirmed. The binding analysis suggests close interactions of the dsRNA with PHE228, ASN261, ARG271, PRO295, and LYS298. These results agree with previous experimental and simulation-based studies, which report PHE228, ARG271, ARG294, and LYS298 as the important residues for dsRNA binding, and mutations in these residues are reported to reduce dsRNA binding affinity [48]. The remaining site was confirmed to have strong interactions with RdRp **(Figure 2)** and was assigned to be the RdRp binding domain (RdRpD).

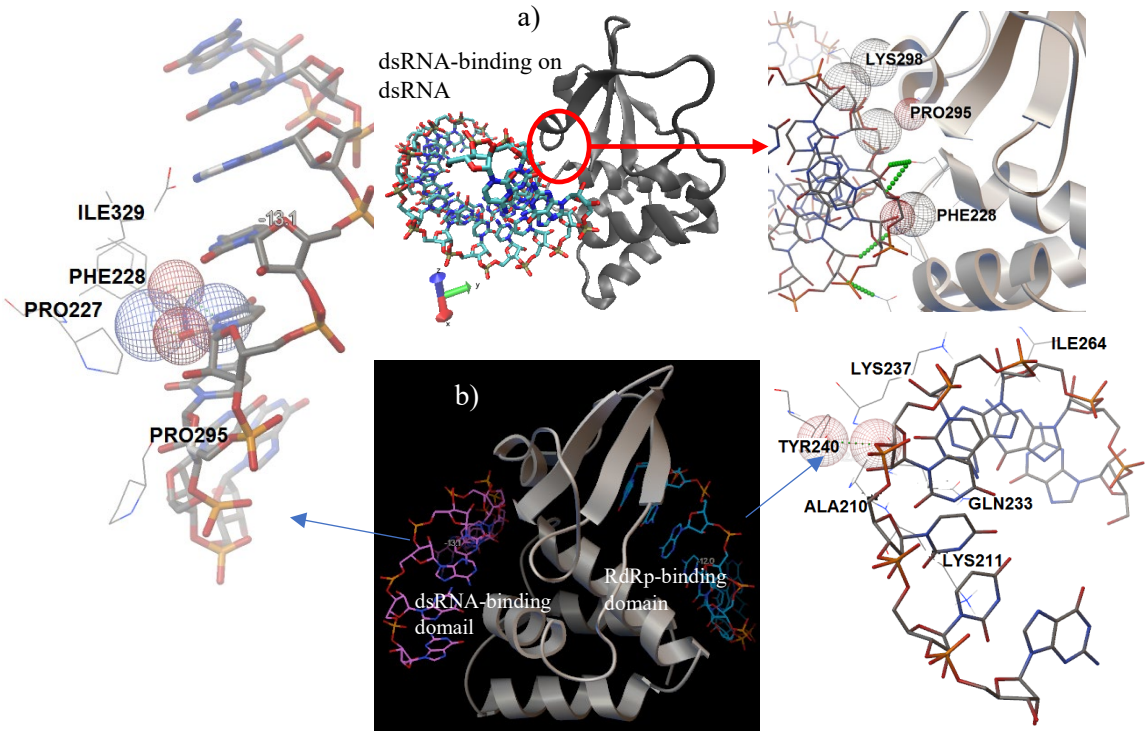

Figure 2. a) Double-stranded RNA (dsRNA) interactions with Marburg virus VP35 polymerase; b) Binding phenomena of single-stranded (ssRNA) with VP35 showing interactions at both dsRNA and RdRp binding domains. H-bonding depicted in green whereas close interactions are denoted in gridded circles.

Since the ultimate objective of this analysis was to come up with potential viral inhibitors, it was decided to interrogate the protein with nucleotides of decreasing complexity. Accordingly, a docking simulation was done on VP35 initially with an 11-base ssRNA [35]. This analysis confirms the preferential binding of ssRNA to dsRNA site with a binding affinity of -13.1 kcal/mol while also confirming the binding ability of ssRNA to RdRpD with a lower, but significant affinity of -12.1 kcal/mol **(Figure 2c)**, suggesting the susceptibility of both sites to RNA-analog-based inhibition. Obviously, ssRNAs are unlikely candidates as antiviral drugs owing to their large size; nevertheless, nucleotide triphosphate (NTP) and oligonucleoside triphosphate (OTP) analogs are promising candidates as target drugs. Accordingly, as the next step, how RNA NTPs interact with the VP35 was investigated.

NAMD simulations with the four RNA NTPs revealed that the interaction space broadens significantly from two (dsRNA and RdRp binding sites in the case of double and single-stranded RNA) to three that included an additional NTP-binding domain (NTPD) **(Figure 3)**. Of the NTPs, analysis of binding energies suggests that adenosine triphosphate (ATP) and uridine triphosphate (UTP) have a binding preference to dsRNA and RdRp-binding domains; however, all four nucleotides displayed a high affinity multi-conformational binding preference to NTPD at the vicinity of residues THR272, PHE273, and ASP274. The positioning of the NTPD on 4GHA with the coiled-coil region of VP35 (5TOI) suggests this site plays a role in routing the NTPs to the oligomerization domain of VP35 **(Figure 1b)**.

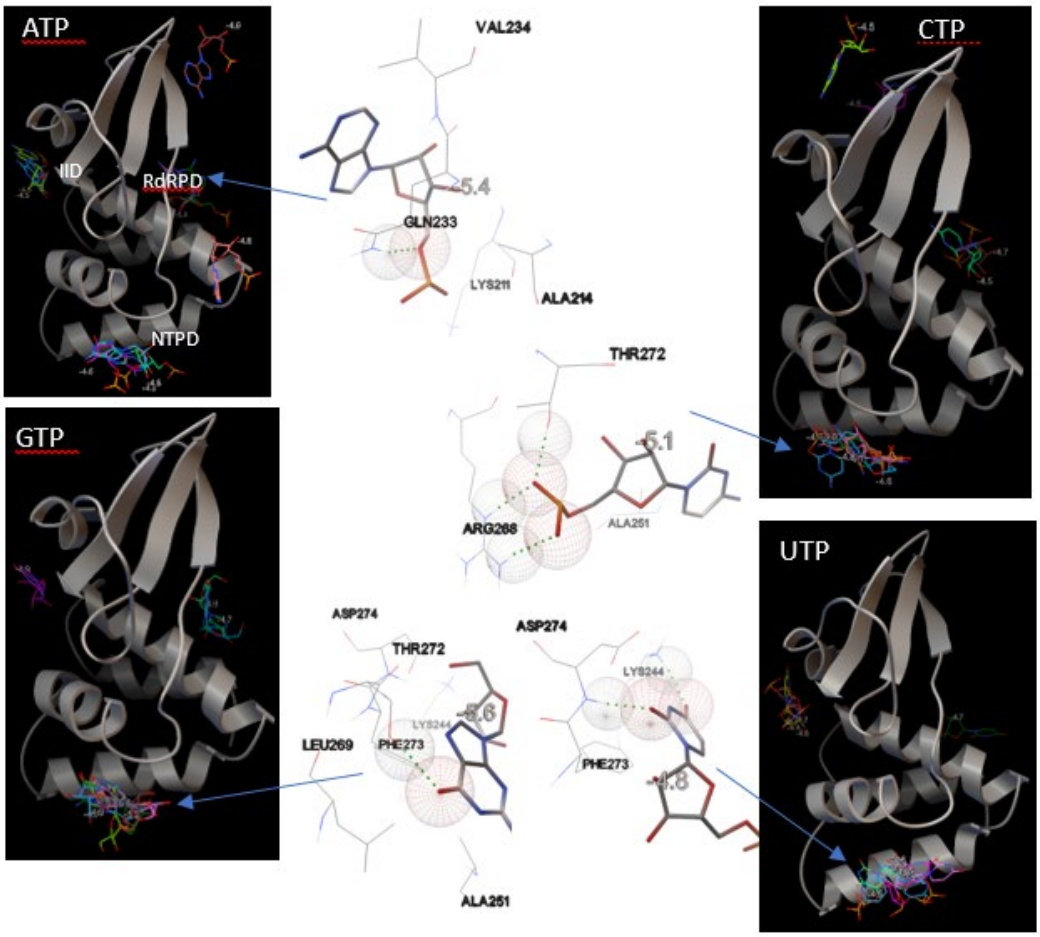

Figure 3. RNA nucleotide interactions with Marburg virus VP35 polymerase; A – adenosine, C-cytosine, G-guanidine, and U-uracil triphosphates.

Druggability Assessment

The druggability of VP35 was assessed via NAMD simulations in the presence of drug-like inorganic probe molecules. The system setup of protein in a solution of probe molecules is shown in **Figure 4a**. The druggability assessment of VP35 revealed the presence of 75 small molecule binding hotspots (ΔG = -2.71 to -1.00 kcal/mol) of which 46 binding hotspots were recognized for isopropanol with the lowest ΔG of -2.60 kcal/mol. However, other probe molecules like isobutene (11 hotspots, -2.00 kcal/mol), isopropylamine (1 hotspot; -2.71 kcal/mol), acetamide (3 hotspots, -1.46 kcal/mol), and acetate (14 hotspot, -1.89 kcal/mol) were more remote. The analysis predicted one druggable site that coincided with the dsRNA binding domain IID-I **(Figure 4b)** with a binding free energy of -12.74 kcal/mol and the highest affinity of 0.513 nM for a drug-like molecule occupying a volume of 475.37 A^3 on the receptor surface.

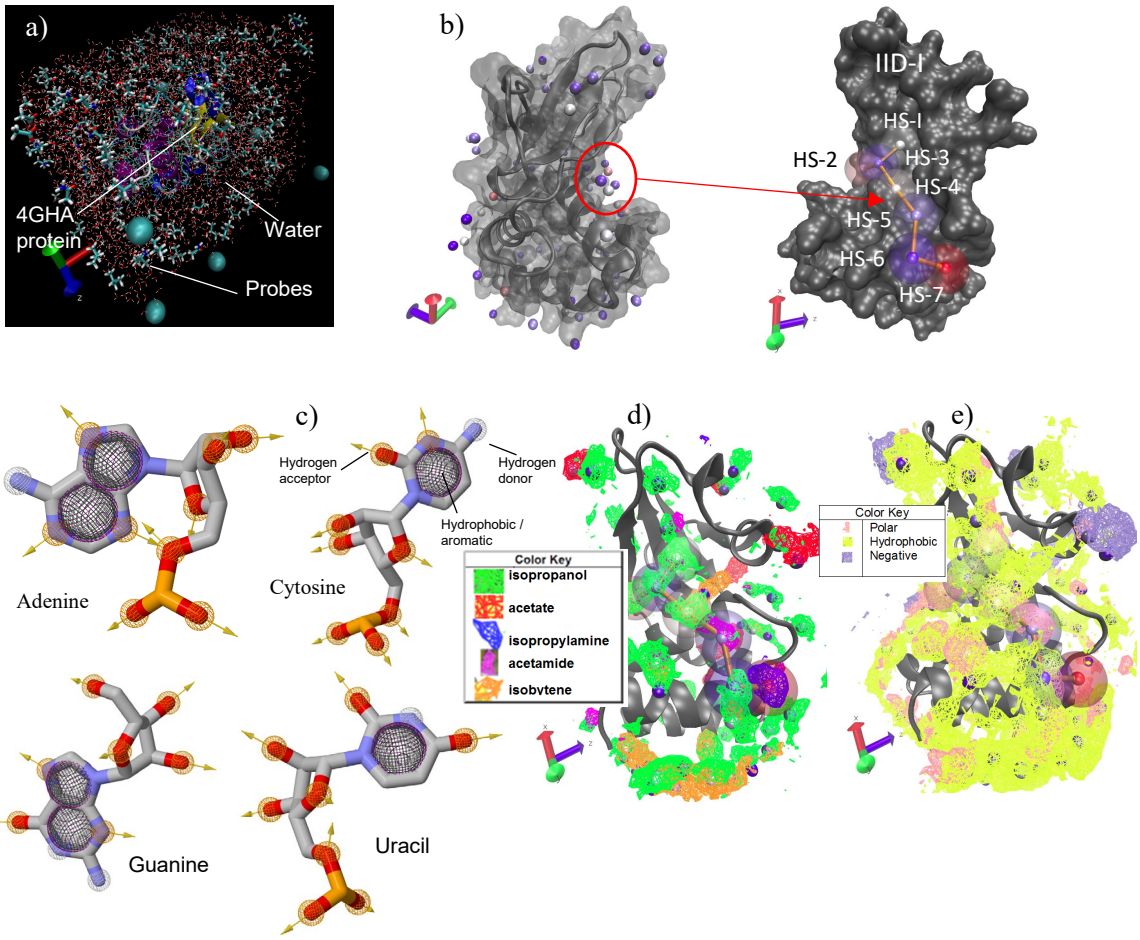

Figure 4. a) probe interactions with Marburg virus VP35 polymerase. b) druggable sites at dsRNA binding domain IID-I. c) The pharmacophore point analysis of the NTP ligands. d) The pharmacophore point distribution of the NTP ligands and VP35 receptor. e) The VP35 protein surface properties. The analysis revealed a cluster of seven hotspots at the vicinity of dsRNA and RdRp domains.

Pharmacophore Identification

Once the druggability of the protein was confirmed, the pharmacophore points were isolated via ligand analysis and dynamic receptor analysis using ELIXIR-A. The pharmacophore points of the four ligands are depicted in **Figure 4c**. As can be seen, the primary pharmacophore points for the ligand system consisted of hydrogen acceptors, hydrogen donors, and hydrophobic/aromatic.

The pharmacophore distribution of the VP35 receptor is depicted in **Figure 4b**. It could be noted that from the probes tested, the ones that bound at the vicinity of the dsRNA receptor was isopropanol on hotspots (HS) 1, 2, 3, 4, and 6, followed by acetamide (HS 5) and isopropylamine (HS 7) at the bottom-most hotspot in the seven-hotspot cluster **(Figures 4b and 4d)**. The distribution of polar, negatively charged, and hydrophobic pharmacophores is depicted in **Figure 4e**. As could be seen, hotspots HS1-4 also displayed affinity toward hydrophobic groups while HS1, 2, and 4 showed a high affinity to polar groups.

Compound Screening and Verification

Ligand screening via the ZINCPharmer facility resulted in three potential ligands, an ATP analog 3-[(2-carbamoyl-1-benzofuran-3-yl)sulfamoyl]-4-methyl benzoic acid (CBSMA, ZINC23883422); [(2S,3R,4S,5S,6S)-2-[5,7-dihydroxy-2-(4-hydroxyphenyl)-4-oxo-chromen-3-yl]oxy-3-hydroxy-5-[(E)-3-(4-) (DOCHE, ZINC137664569); and 7,7'-Nonane-1,9-diylbis[estra-1,3,5(10)-triene-3,17β-diol (Fulvestrant Impurity D, FID, ZINC77311906), an analog of the chemotherapy agent Fulvestrant with a high similarity to select pharmacophores of the ligand-receptor combination. The FID conformations of the highest binding affinity are depicted in **Figure 5a**. This ligand occupies a large volume of the binding pocket (377.6 A^3), providing the highest likelihood of being a potent inhibitor. The binding energies ranged from -6.3 to -5.8 kcal/mol with an estimated drug-like affinity of 34.846 uM. Remarkably, the simulations predict that, unlike the other two candidates, FID binds strongly to the triad of dsRNA binding, RdRp binding, and NTP binding domains with binding free energies of -6.3, -6.1, and -5.1 kcal/Mol, respectively **(Figure 5b)**. The other candidates are bound only to the dsRNA and NTP binding domains.

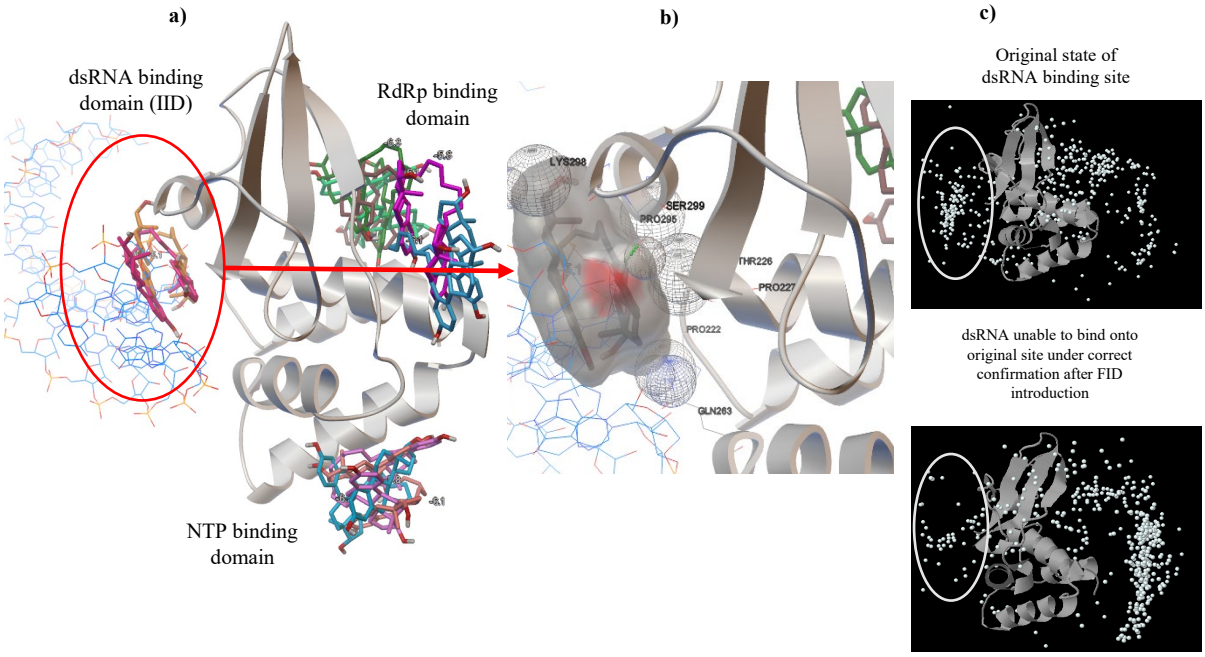

Figure 5. a) Binding confirmations of impurity D of Fulvestrant anticancer drug on VP35 showing its versatility in binding onto dsRNA, RdRp and NTP binding domains; b) The fate of dsRNA prior to and after FID introduction depicting the ligand's efficacy on preventing dsRNA binding onto the original active site of VP35. Once bound FID assumes a "U" shaped pincer like conformation occupying a large volume of the active site causing steric hinderance and by making the site hydrophobic, shielding substrate binding. Fulvestrant class of drugs are known to bind onto the estrogen receptor proteins of metastatic breast cancer cells by making the site hydrophobic and destabilizing it, causing the cell's normal degradation processes to destroy the protein.

Simulations with dsRNA and VP35 before and after FID addition revealed that once FID is introduced, dsRNA could not bind onto the original dsRNA binding site on its capping confirmation **(Figure 5b)**. This revelation is promising since FID can thwart the immunosuppressive mechanism that the virus uses to evade our body's immune response.

Simulations done to ascertain the impact of FID introduction on the RdRpD on VP35 revealed that the RdRp binding landscape was significantly altered as a result of FID introduction. A closer look at the binding conformations reveals that RdRp did no longer bind to the original active site in its preferred conformations **(Figure 6)**.

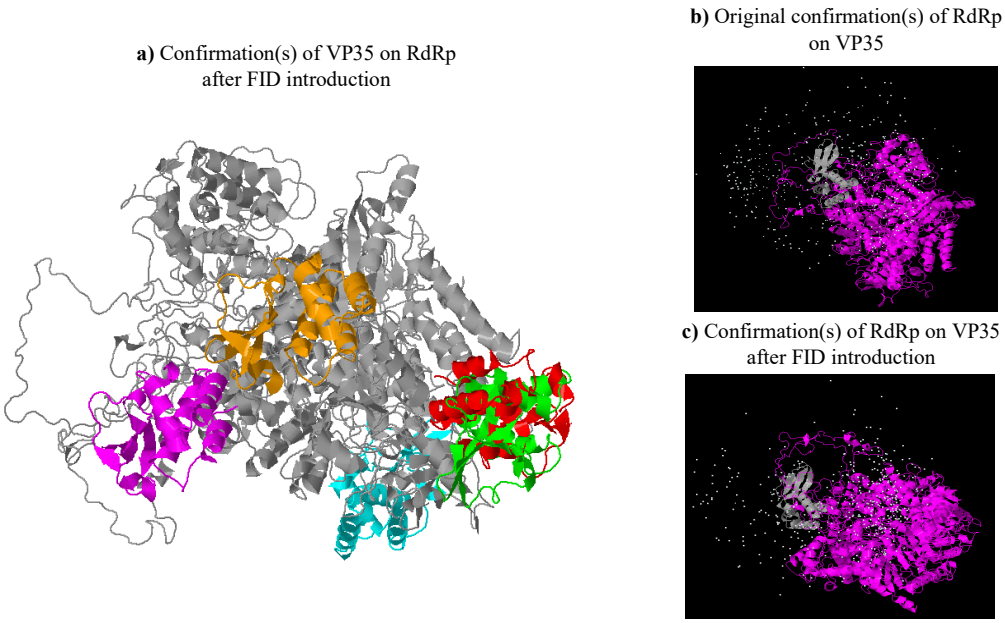

Figure 6. a) Confirmation(s) of VP35 on RdRp after FID introduction. The binding landscape has changed significantly after FID introduction as compared to Figure 1a; b) Confirmation(s) of RdRp on VP35 before and c) after attachment of FID. The dotted diagrams depict the spread of the 500 most stable confirmations of RbRp on VP35 corroborating a significant alteration of the binding preference and conformations of RdRp on VP35 after FID ligand attachment.

FID binding onto NTPD with high affinity (-6.3 kcal/mol) indicates a fortuitous outcome of the ability of FID to bind much tighter to the pocket than any of the NTPs (i.e., GTP -5.6, CTP -4.9, ATP -4.8, and UTP -4.8 kcal/mol) thwarting oligomerization at the coiled-coil region of VP35. None of the other ligands tested displayed this unique efficacy by binding with consistently high affinities across all three sites.

Intermolecular Interaction Analysis from MD Simulation

The stability of the ligand-receptor binding complex was further validated by MD simulations. The RMSD values during the 20 ns simulation reflect the conformational changes of the complexes in the neutral solvent solution system. The RMSD values for the proteins were 1.273 ± 0.238 Å, 1.236 ± 0.169 Å, and 1.130 ± 0.185 Å for the complex of CBSAMA, DOCHE, and FID, respectively **(Figure 7a)**. The standard deviations for all simulations were between 0.15 and 0.25 Å, indicating that all protein-ligand complexes did not undergo large confirmatory changes during the simulations. The RMSF values of each amino acid in the complex of CBSAMA, DOCHE, and FID were between 0.3 and 2.5 Å. The abnormally high RMSF values come from the C and N terminals.

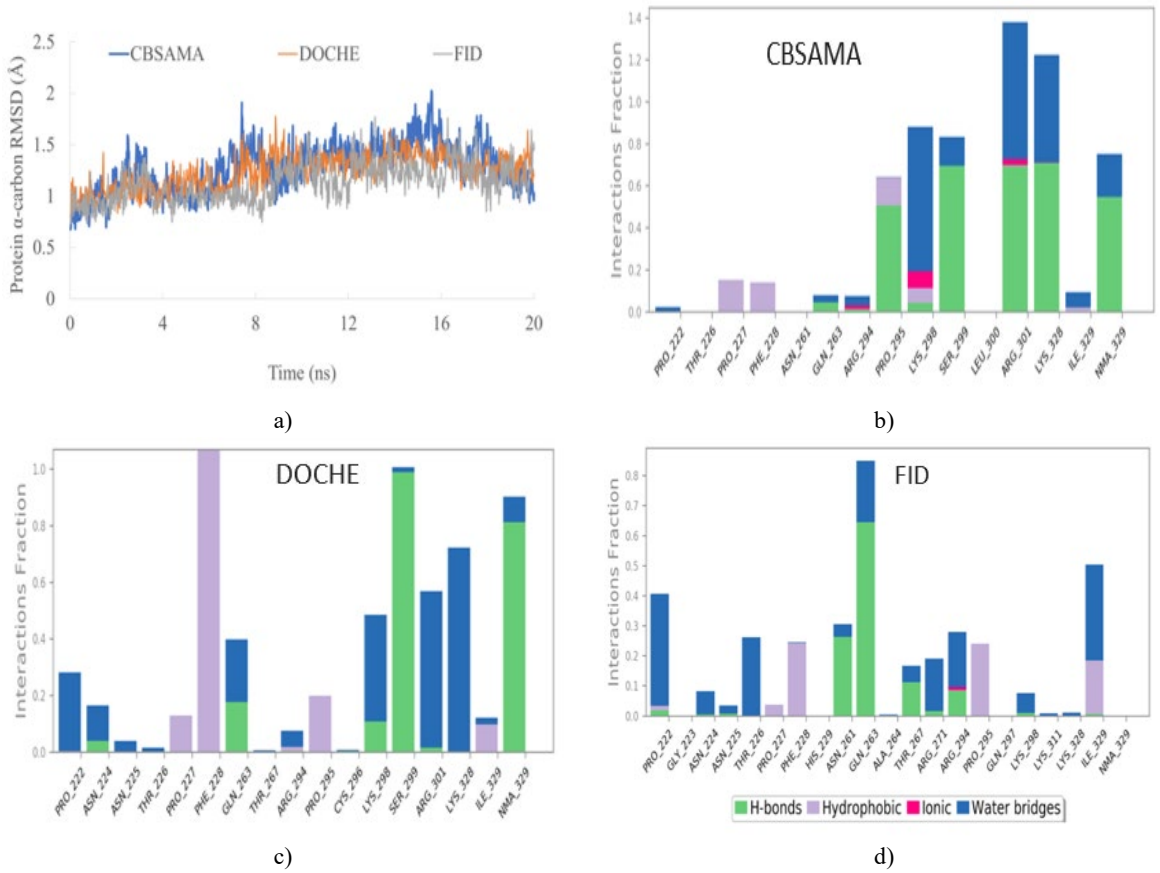

Figure 7. a) Protein α-carbon RMSD plot of Marburg VP35 protein complexed with ligands. b, c, and d) Protein-ligand interactions plot of Marburg VP35 protein complexed with CBSAMA, DOCHE, and FID. Four different types of non-covalent contacts (H-bonds, hydrophobic, ionic, and water bridges) were obtained from the simulation.

The protein-ligand plots help to reveal the change of interactions during the simulation. This analysis shows the binding modes of the ligands interacting with the dsRNA binding domain IID. Among the four monitored non-covalent contacts, H-bonds were known to significantly influence the drug specificity in binding. Therefore, H-bonds would be considered to a greater extent when assessing the performance of protein-small molecule interactions.

In the VP35/CBSMA complex **(Figure 7b)**, four major H-bonds (>50% occupancy) were formed, including amino acids PRO295, SER299, ARG301, LYS328. Since NMA329 was a covered N-terminal, it was not included in this analysis. The two amino acids ARG301 and LYS328 not only H-bonds interacted but also formed water bridges (>30%), which resulted in a total interaction fraction greater than one. In the VP35/DOCHE complex **(Figure 7c)**, the major interaction was a hydrophobic binding with PHE228 (>100%) and a H-bond interaction with SER299 (>90%). In the VP35/FID complex **(Figure 7d)**, two major H-bonds with ASN261 (>20%) and GLN263 (>60%) were formed. Three amino acids, PHE228, PRO295, and ILE329, formed hydrophobic contacts and contributed about 20% of the overall simulation. Based on the analysis of intermolecular interactions, all three molecules were able to remain on the dsRNA binding domain IID with strong H-bonds. CBSMA and DOCHE formed strong H-bond interactions that showed good specificity in the IID region.

Conclusion

Using nucleoside triphosphates, specific sites within the VP35 that have a high affinity to dsRNA, RdRp, and NTPs were identified. NTP-based interrogations revealed the affinity of key domains of VP35, i.e., dsRNA, RdRp, and NTP-binding domains to NTP-analogs. Further interrogations with drug-like model probes using molecular dynamic simulations revealed that these domains of VP35 have a high enough affinity to drug-like molecules indicating that VP35 is, in fact, druggable. Studies revealed a cluster of hotspots that spanned the dsRNA, RdRp, and NTP binding domains. Using the pharmacophore points identified from NTP and dynamic receptor analysis, three potential drug molecules were uncovered. CBSMA and DOCHE showed good potential with the specificity in the IID region. Interestingly, FID, an estrogen receptor antagonist antineoplastic chemotherapy agent, proved to have a remarkable affinity to all three domains of VP35. Consequently, FID can potentially suppress the dsRNA capping ability responsible for immunosuppression, preventing RdRp binding and thwarting NTP routing to the oligomerization domain – a remarkable feat if confirmed by experimental validations. The ability of chemotherapeutic agents to bind onto rapidly proliferating viruses is not tenuous since the mission of these agents in human cancer cells is analogous. This work only lays the groundwork on the possibility of using this class of chemicals as a defense against an equally lethal line of hosts – the viruses.

Acknowledgments: The authors gratefully acknowledge the support from Texas A&M High Performance Research Computing (HPRC) and Laboratory for Molecular Simulation (LMS).

Conflict of interest: None

Financial support: The authors acknowledge partial support received from Texas A&M Agrilife Research for this work.

Ethics statement: None

References

1. Bioterrorism Agents/Diseases [Internet]. Available from: https://emergency.cdc.gov/agent/agentlist-category.asp#a
2. NIAID Emerging Infectious Diseases/ Pathogens [Internet]. Available from: https://www.niaid.nih.gov/research/emerging-infectious-diseases-pathogens
3. Ristanović ES, Kokoškov NS, Crozier I, Kuhn JH, Gligić AS. A forgotten episode of Marburg virus disease: Belgrade, Yugoslavia, 1967. Microbiol Mol Biol Rev. 2020;84(2):e00095-19.
4. Olejnik J, Mühlberger E, Hume AJ. Recent advances in marburgvirus research. F1000Res. 2019;8:F1000 Faculty Rev-1704.
5. Nyakarahuka L, Shoemaker TR, Balinandi S, Chemos G, Kwesiga B, Mulei S, et al. Marburg virus disease outbreak in Kween District Uganda, 2017: Epidemiological and laboratory findings. PLoS Negl Trop Dis. 2019;13(3):e0007257.
6. Languon S, Quaye O. Filovirus disease outbreaks: a chronological overview. Virology. 2019;10:1178122X19849927.
7. Talisuna AO, Okiro EA, Yahaya AA, Stephen M, Bonkoungou B, Musa EO, et al. Spatial and temporal distribution of infectious disease epidemics, disasters and other potential public health emergencies in the World Health Organisation Africa region, 2016-2018. Glob Health. 2020;16(1):1-12.
8. Cooper TK, Sword J, Johnson JC, Bonilla A, Hart R, Liu DX, et al. New Insights Into Marburg Virus Disease Pathogenesis in the Rhesus Macaque Model. J Infect Dis. 2018;218(suppl_5):S423-33.
9. Shifflett K, Marzi A. Marburg virus pathogenesis – differences and similarities in humans and animal models. Virol J. 2019;16(1):165.
10. Bhat SH, Ullah MF, Abu-Duhier FM. Anti-hemolytic Activity and Antioxidant Studies of Caralluma quadrangula: Potential for Nutraceutical Development in Cancers and Blood Disorders. Int J Pharm Res Allied Sci. 2019;8(4):121-9.
11. Bauer MP, Timen A, Vossen AC, van Dissel JT. Marburg haemorrhagic fever in returning travellers: an overview aimed at clinicians. Clin Microbiol Infect. 2019;21:e28-e31.
12. Reynolds P, Marzi A. Ebola and Marburg virus vaccines. Virus Genes. 2017;53(4):501-15.
13. Kurdi L, Alhusayni F. Cytotoxicity effect of 5-fluorouracil and bee products on the MCF-7 Human Breast Cancer Cell Line in vitro. Int J Pharm Phytopharmacol Res. 2020;10(2):19-26.
14. Dulin N, Spanier A, Merino K, Hutter JN, Waterman PE, Lee C, et al. Systematic review of Marburg virus vaccine nonhuman primate studies and human clinical trials. Vaccine. 2020;39(2):202-8.
15. Wijesinghe KJ, Urata S, Bhattarai N, Kooijman EE, Gerstman BS, Chapagain PP, et al. Detection of lipid-induced structural changes of the Marburg virus matrix protein VP40 using hydrogen/deuterium exchange-mass spectrometry. J Biol Chem. 2017;292(15):6108-22.
16. Bhattarai N, Gerstman BS, Chapagain PP. Role of k-loop cysteine residues in the marburg virus protein VP24–human Keap1 complex. ACS Omega. 2018;3(12):18639-45.
17. Tigabu B, Ramanathan P, Ivanov A, Lin X, Ilinykh PA, Parry CS, et al. Phosphorylated VP30 of Marburg virus is a repressor of transcription. J Virol. 2018;92(21):e00426-18.

18. Tchesnokov EP, Feng JY, Porter DP, Götte M. Mechanism of inhibition of Ebola virus RNA-dependent RNA polymerase by remdesivir. Viruses. 2019;11(4):326.
19. Bruhn JF, Kirchdoerfer RN, Urata SM, Li S, Tickle IJ, Bricogne G, et al. Crystal Structure of the Marburg Virus VP35 Oligomerization Domain. J Virol. 2017;91(2):e01085-16.
20. Oda S-i, Noda T, Wijesinghe KJ, Halfmann P, Bornholdt ZA, Abelson DM, et al. Crystal structure of Marburg virus VP40 reveals a broad, basic patch for matrix assembly and a requirement of the N-terminal domain for immunosuppression. J Virol. 2016;90(4):1839-48.
21. Luthra P, Anantpadma M, De S, Sourimant J, Davey RA, Plemper RK, et al. High-Throughput Screening Assay to Identify Small Molecule Inhibitors of Marburg Virus VP40 Protein. ACS Infect Dis. 2020;6(10):2783-99.
22. Liu B, Dong S, Li G, Wang W, Liu X, Wang Y, et al. Structural insight into nucleoprotein conformation change chaperoned by VP35 peptide in Marburg virus. J Virol. 2017;91(16):e00825-17.
23. Zhu T, Song H, Peng R, Shi Y, Qi J, Gao GF. Crystal structure of the Marburg virus nucleoprotein core domain chaperoned by a VP35 peptide reveals a conserved drug target for filovirus. J Virol. 2017;91(18):e00996-17.
24. Hume A, Mühlberger E. Marburg Virus Viral Protein 35 Inhibits Protein Kinase R Activation in a Cell Type–Specific Manner. J Infect Dis. 2018;218(suppl_5):S403-8.
25. Edwards MR, Liu G, Mire CE, Sureshchandra S, Luthra P, Yen B, et al. Differential Regulation of Interferon Responses by Ebola and Marburg Virus VP35 Proteins. Cell Rep. 2016;14(7):1632-40.
26. Bale S, Julien JP, Bornholdt ZA, Kimberlin CR, Halfmann P, Zandonatti MA, et al. Marburg virus VP35 can both fully coat the backbone and cap the ends of dsRNA for interferon antagonism. Plos Pathog. 2012, 8(9):e1002916.
27. Olejnik J, Hume AJ, Leung DW, Amarasinghe GK, Basler CF, Mühlberger E. Filovirus strategies to escape antiviral responses. Marbg Ebolaviruses 2017;411:293-322.
28. Geer LY, Marchler-Bauer A, Geer RC, Han L, He J, He S, et al. The NCBI biosystems database. Nucleic Acids Res. 2010;38(suppl_1):D492-6.
29. Amatya P, Wagner N, Chen G, Luthra P, Shi L, Borek D, et al. Inhibition of Marburg Virus RNA Synthesis by a Synthetic Anti-VP35 Antibody. ACS Infect Dis. 2019;5(8):1385-96.
30. Cross RW, Mire CE, Feldmann H, Geisbert TW. Post-exposure treatments for Ebola and Marburg virus infections. Nat Rev Drug Discov. 2018;17(6):413-34.
31. UniProtKB - P31352 (L_MABVM)
32. Pierce BG, Wiehe K, Hwang H, Kim BH, Vreven T, Weng Z. ZDOCK server: interactive docking prediction of protein–protein complexes and symmetric multimers. Bioinformatics. 2014;30(12):1771-3.
33. Trott O, Olson AJ. Software News and Update AutoDock Vina: Improving the Speed and Accuracy of Docking with a New Scoring Function, Efficient Optimization, and Multithreading. J Comput Chem. 2010;31(2):455-61.
34. Morris GM, Huey R, Lindstrom W, Sanner MF, Belew RK, Goodsell DS, et al. AutoDock4 and AutoDockTools4: Automated docking with selective receptor flexibility. J Comput Chem. 2009;30(16):2785-91.
35. Trott O, Olson AJ. AutoDock Vina: improving the speed and accuracy of docking with a new scoring function, efficient optimization, and multithreading. J Comput Chem. 2010;31(2):455-61.
36. Bakan A, Nevins N, Lakdawala AS, Bahar I. Druggability Assessment of Allosteric Proteins by Dynamics Simulations in Presence of Probe Molecules. Biophys J. 2013;104(2):556a.
37. Phillips JC, Hardy DJ, Maia JD, Stone JE, Ribeiro JV, Bernardi RC, et al. Scalable molecular dynamics on CPU and GPU architectures with NAMD. J Chem Phys. 2020;153(4):044130.
38. Wang H, Jayaraman A, Menon R, Gejji V, Karthikeyan R, Fernando S. A non-beta-lactam antibiotic inhibitor for enterohemorrhagic Escherichia coli O104: H4. J Mol Med. 2019;97(9):1285-97.
39. Fernando S, Fernando T. Antivirals for allosteric inhibition of Zika virus using a homology model and experimentally determined structure of envelope protein. BMC Res Notes. 2017;10(1):354.
40. Gejji V, Svoboda P, Stefanik M, Wang H, Salat J, Eyer L, et al. An RNA-dependent RNA polymerase inhibitor for tick-borne encephalitis virus. Virology. 2020;546:13-9.
41. Mulgaonkar N, Wang H, King M, Fernando S. Druggability assessment of precursor membrane protein as a target for inhibiting the Zika virus. J Biomol Struct Dyn. 2020:1-17.
42. Koes DR, Camacho CJ. ZINCPharmer: pharmacophore search of the ZINC database. Nucleic Acids Res. 2012;40(W1):W409-14.
43. Sterling T, Irwin JJ. ZINC 15–ligand discovery for everyone. J Chem Inf Model. 2015;55(11):2324-37.
44. Release S. 4: Desmond molecular dynamics system. DE Shaw Research: New York, NY. 2017.
45. Wizard PP, Epik S. LLC. New York, NY. 2019.
46. Glide S. LLC. New York, NY. 2017.
47. Roos K, Wu CJ, Damm W, Reboul M, Stevenson JM, Lu C, et al: OPLS3e: Extending Force Field Coverage for Drug-Like Small Molecules. J Chem Theory Comput. 2019;15(3):1863-74.
48. Sponer J, Bussi G, Krepl M, Banáš P, Bottaro S, Cunha RA, et al. RNA structural dynamics as captured by molecular simulations: a comprehensive overview. Chem Rev. 2018;118(8):4177-338.